Weighted Factor Multiobjective Design Optimization of a Reluctance Synchronous Machine

Eduan Howard, *Student Member, IEEE*, and Maarten J. Kamper, *Senior Member, IEEE*

***Abstract*—The relationship between the well-known competitive torque density and less-competitive power factor of reluctance synchronous machines (RSMs) is investigated in this study. The investigation was carried out by implementing a complete machine model in the optimization, with varying machine-pole number and flux-barrier number combinations. Furthermore, the study consists of a multiobjective design optimization implementing a weighted-factor optimization technique. Determination of the weighting of this specific parameter relationship enables the designer to select an optimum multiobjective relationship during optimization. A specific machine was selected for analysis, then analyzed and manufactured for validation of simulation results.**

***Index Terms*—Asymmetric pole structure, finite-element (FE) analysis, flux barrier, multiobjective optimization, optimization algorithms, synchronous reluctance machine, weighted factor optimization.**

I. Introduction

DUE to the increasing interest in more efficient and cost-effective drives in the electrical machine market, research into reluctance synchronous machines (RSMs) has intensified. This is due to the well-known high efficiency of RSMs, with a much simpler rotor topology compared to induction and permanent-magnet machines. The significant drawback of RSMs is, however, its low competitive power factor, with an increase in required inverter power rating and, hence, a higher machine inverter-drive package cost.

A critical part in the design of an RSM is the shaping of the flux barriers. This topic has attracted much attention in literature as illustrated in a few recent example studies [1]–[7]. The focus of the majority of the studies that have been conducted is on the maximization of torque within a constrained volume [8], the minimization of torque ripple [2], [9], [10], or a combination of the two [1]. However, there is limited literature describing investigations into the effect that variation of the number of flux barriers and the flux-barrier shape has on other machine parameters, such as the power factor (P_F).

In order to study this inherent disadvantage of RSMs, this paper describes an investigation into the relationship between P_F and the relatively competitive torque density commonly achieved in RSMs. The method of analysis implements a numeric design optimization process to investigate the effects that the flux-barrier number and shape variation, machine-pole number, and power-level variation have on the average torque (T_A) and P_F relationship. This relationship is determined by implementing a weighted-sum (or scalarization) method that solves a multiple-objective optimization problem by combining the respective objectives into one single-objective function. With the objective functions

Manuscript received July 16, 2015; revised September 24, 2015; accepted October 14, 2015. Date of publication February 19, 2016; date of current version May 18, 2016. Paper 2015-EMC-0580.R1, presented at the 2015 IEEE International Electric Machines and Drives Conference, Coeur d'Alene, ID, USA, May 10–13, and approved for publication in the IEEE TRANSACTIONS ON INDUSTRY APPLICATIONS by the Electric Machines Committee of the IEEE Industry Applications Society.This work was supported by ABB Corporate Research, Sweden.

The authors are with the Department of Electrical and Electronic Engineering, Stellenbosch University, Stellenbosch 7602, South Africa (e-mail: eduanhoward@telkomsa.net; kamper@sun.ac.za).

Color versions of one or more of the figures in this paper are available online at http://ieeexplore.ieee.org.

Digital Object Identifier 10.1109/TIA.2016.2532287

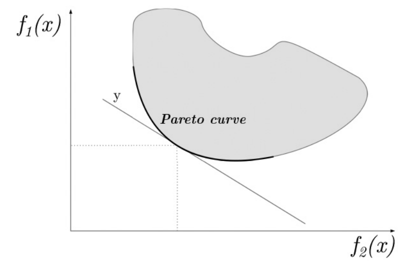

Fig. 1. Illustration of the pareto front construction by implementing the scalarization method to solve multiobjective optimization problems.

$$y = \gamma_1 f_1(x) + \gamma_2 f_2(x) \tag{1}$$

as presented in Fig. 1, represented by $f_1(x)$ as T_A and $f_2(x)$ as P_F. The objective function is determined by shifting the respective weighted factors from T_A to P_F, with the weighted factors represented by γ_1 and γ_2, respectively, with

$$\gamma_2 = 1 - \gamma_1 \tag{2}$$

and with

$$0 \leqslant \gamma_1 \leqslant 1 \tag{3}$$

and

$$0 \leqslant \gamma_2 \leqslant 1. \tag{4}$$

The model for flux-barrier creation implemented in the design optimization process is reported in literature [11]. In this paper, an alternative flux-barrier-creation technique is described that implements an asymmetric pole structure in conjunction with an extensively variable flux-barrier topology is described. An illustration of this asymmetric structure is presented in Fig. 2(c). The motivation for implementing this asymmetric structure is twofold. First, a 50% (on average) reduction in torque ripple can be achieved with this asymmetric pole topology as compared to a symmetric topology, as described in

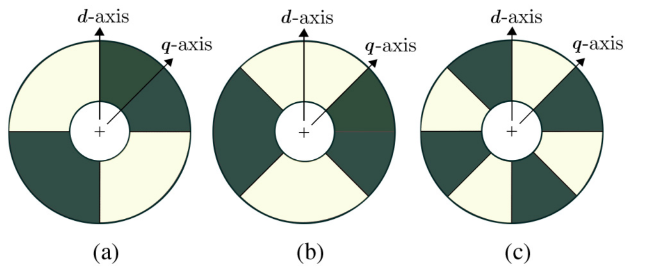

Fig. 2. Four-pole asymmetric structure illustrating the different pole topologies [11]. (a) Asymmetric rotor structure about the d-axis with symmetric q-axis. (b) Asymmetric rotor structure about the q-axis with symmetric d-axis. (c) Asymmetric rotor structure about the q- and d-axes.

[11], with similar results reported in [2]. Second, as one of the aims of this study was to investigate the effects across a varying machine-pole range, a flux-barrier topology that can easily adapt to a large range of machine-pole numbers is required.

The main advantage that the asymmetric topology has over the alternative conventionally implemented asymmetric topology [Fig. 2(a) and (b)] is that only one machine pole needs to be modeled in the finite-element (FE) package, compared to the two poles required for the alternative asymmetric pole topology. This reduction in the required FE model size subsequently reduces the optimization time by reducing the respective simulation time per optimizer function call.

The main disadvantage of this topology, however, is its potential performance parameter variation under varying machine-operation modes and the direction of rotation. In this study, a unidirectional mode of operation that is applicable to, e.g., generators, pumps, and conveyor drives is assumed.

This paper consists of seven sections. In Section II, the machine model implemented in the design process is presented. Section III describes the performance parameter calculations. In Section IV, the optimization process and strategies implemented are presented. The weighted-factor optimization study is described in Section V. For the purpose of validation, a machine that emanated from this study's results was selected for manufacture, and these results are discussed in Section VI. Finally, the conclusion is presented in Section VII.

II. Machine Model

The implemented flux barrier, presented in [11], is shown in Fig. 3(a) and (b). Eight variables were implemented to create one flux barrier, given by

$$X_R = \left[\alpha_L \ \alpha_R \ \beta_L \ \beta_R \ R \ P_{1sp} \ P_{3sp} \ P_{5sp}\right]^T \tag{5}$$

with the web width of the flux barriers chosen as a fixed 0.5 mm during the optimization. This minimum width is selected based on manufacturing constraints, where for punching of the lamination, the web width must not be less than the thickness of the lamination.

In addition, in order to accurately model the weighted values between P_F and T_A, the stator design is also optimized. The stator-slot design points are illustrated in Figs. 4 and 5, with the point variables tabulated in Table I. The stator construction

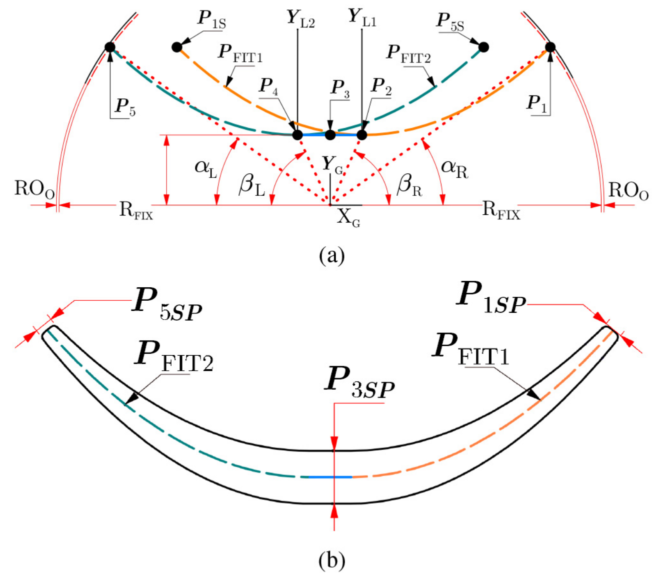

Fig. 3. Asymmetric flux-barrier model presented in [11].

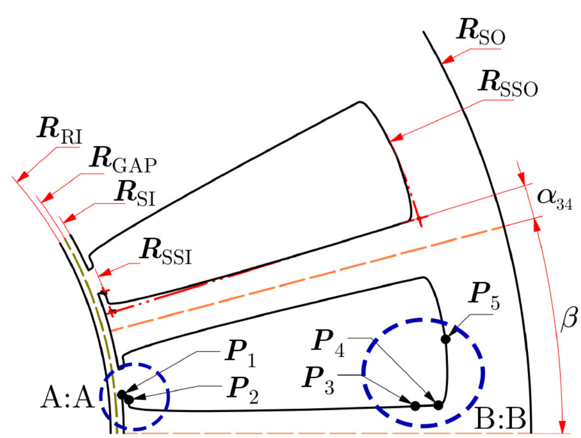

Fig. 4. Main stator-slot design points.

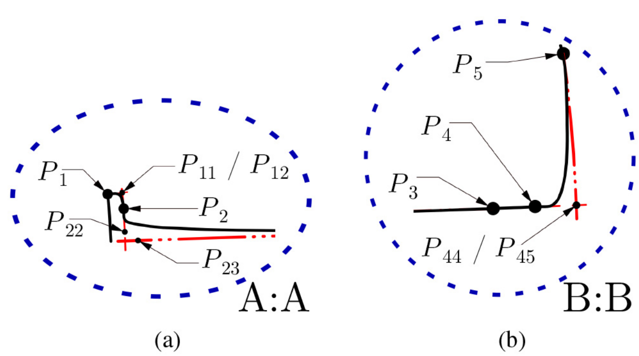

Fig. 5. Illustration of stator-slot tip and base variable points. (a) Slot tip. (b) Slot base.

consists of three bézier cubic spline fittings, the first of which is from point P_1 to P_2, the second from P_2 to P_3, and the final from point P_4 to P_5. A straight line connects points P_3 and P_4.

Furthermore, the spline departure and arrival points are fixed. They are represented by points P_{11} and P_{12} for points P_1 and P_2, points P_{22} and P_{23} for points P_2 and P_3, and finally, points P_{44} and P_{45} for points P_4 and P_5, as shown in Fig. 5(a) and (b).

TABLE I
STATOR-SLOT VARIABLES

Stator main points		
Polar	R	θ
P_1	$R_{P_1} = R^{\star}_{\mathrm{GAP}} + 0.5G_H$	$\theta_{P_1} = \theta_{P_5} - 0.5\theta_{\mathrm{SL}}$
P_2	$R_{P_2} = R^{\star}_{\mathrm{SSI}}$	$\theta_{P_2} = \theta_{P_1} + 0.5(\frac{\theta_{P_5}-\theta_{P_1}}{2})$
P_3	$R^{\star}_{P_3}$	$\theta_{P_3} = \alpha^{\star}_{34}$
P_4	$R^{\star}_{P_4}$	$\theta_{P_4} = \theta_{P_3}$
P_5	$R_{P_5}=R^{\star}_{\mathrm{SSO}}$	$\theta_{P_5} = 0.5\beta$

G_H: air-gap height; θ_{SL}: slot opening; $\beta = \frac{2\pi}{S_p}$; S_p: stator slots per pole; R_{GAP}: air-gap radius; R_{SSI}: slot opening radius; R_{SSO}: slot base radius; $\star$: stator variables.

TABLE II
SPECIFICATIONS AND SOME RATED DATA OF THE RSMs STUDIED

Frame size	P	S_p	B	RO_I (mm)	STO (mm)	L_S (mm)	h (mm)	n (r/min)
90	4	6	$1 \Rightarrow 6$	12.5	65	122	0.3	1500
132	4	9	$1 \Rightarrow 5$	41.0	105	110	0.35	1500
132	6	6	$1 \Rightarrow 6$	41.0	105	110	0.35	1000
132	8	6	$1 \Rightarrow 6$	41.0	105	110	0.35	450

P: number of poles; S_p: stator slots per pole; B: number of flux barriers; RO_I: rotor inside radius; ST_O: stator outside radius; L_S: stack length; h: air-gap height; J: current density = 6.4 A/mm^2.

By varying the radius of points P_3 and P_4, the optimizer has the capability of varying the tooth width and shape of the stator-slot base. The complete set of stator variables consists of seven variables, i.e., six slot dimensions as given in Table I and the current angle θ, as given by

$$X_S = \left[\theta \; R_{\mathrm{GAP}} \; R_{\mathrm{SSI}} \; R_{P_3} \; R_{P_4} \; R_{\mathrm{SSO}} \; \alpha_{34}\right]^T. \tag{6}$$

The machine model was optimized by implementing a constrained model volume that consists of a fixed-stator outside diameter, rotor inside diameter, and stack length. These fixed dimensions were obtained from existing machine frame-size stack dimensions. The specific machine dimensions implemented, along with the respective flux-barrier number per machine analyzed, are given in Table II. During the optimization process, each model implemented standard overlap, full pitch windings, with the stator slots per pole also given in Table II.

III. PARAMETER CALCULATION

The rated current densities implemented in the optimization are given in Table II. The FE simulation package SEMFEM, developed as described in [12], was implemented in the optimization study. The advantage of implementing this package is its script-based user interface, which greatly reduces simulation time.

The power factor is calculated by the well-known power-factor equation

$$P_F = \cos\left(\tan^{-1}\frac{\sigma/\nu + \nu}{\sigma - 1}\right) \tag{7}$$

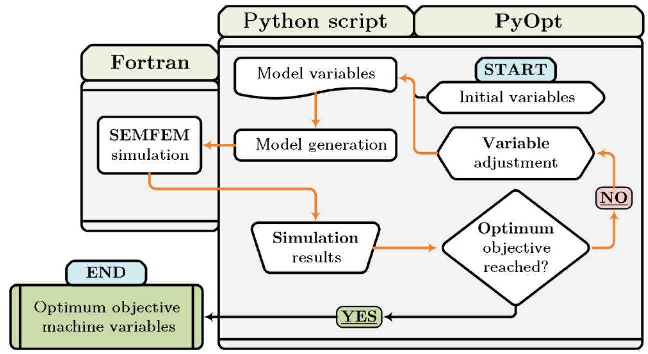

Fig. 6. PyOpt optimization flow diagram.

with

$$\sigma = \frac{L_d}{L_q} \tag{8}$$

$$\nu = \frac{I_q}{I_d} \tag{9}$$

and with

$$L_d = \frac{\lambda_d}{I_d} \tag{10}$$

and

$$L_q = \frac{\lambda_q}{I_q}. \tag{11}$$

In (8)–(11), the parameters λ_q, λ_d, I_q, and I_d are calculated from FE static simulation steps, with the averages of the complete simulation set implemented for each respective variable.

Torque ripple (T_R) is calculated by

$$T_R = \left[\frac{T_{(\mathrm{MAX})} - T_{(\mathrm{MIN})}}{T_A}\right] * 100\% \tag{12}$$

with T_{MAX} and T_{MIN} are the maximum and minimum torque values of the simulated machine, respectively, and T_A is the average simulation torque, with the FE simulation stepped over a 60° electrical angle.

IV. DESIGN OPTIMIZATION

The optimization flow diagram implemented in the study is shown in Fig. 6. The package implemented for the optimization was PyOpt [13], an open-source, Python-based optimization suite. The advantage of implementing PyOpt lies in its open-source availability and script-based user interface, which, in turn, makes optimization flow strategies automatable. This optimization suite is connected to the FE simulation package SEMFEM via a Python script.

Due to the large range of available optimizers that PyOpt provides, an initial algorithm comparison study was conducted to select an optimum optimizer for the specific model. For this optimizer study, six algorithms available in PyOpt were selected as follows:

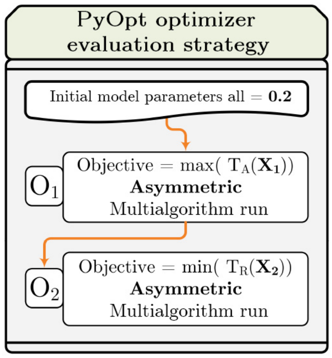

Fig. 7. Optimization strategy to evaluate the selected optimizers in PyOpt.

TABLE III
OPTIMIZATION VARIABLES

Optimization variables		
Variables	X_1	X_2
α_{RL}	√	√
β_{RL}	√	
R	√	
P_{1sp}	√	
P_{3sp}	√	
P_{5sp}	√	
θ	√	
R_{GAP}	√	
R_{SSI}	√	
R_{P_3}	√	
R_{P_4}	√	
R_{SSO}	√	
α_{34}	√	

1) SLSQP—sequential least squares programming;
2) CONMIN—constrained function minimization;
3) SOLVOPT—solver for local optimization problems;
4) KSOPT—Kreisselmeier–Steinhauser optimizer;
5) FILTERSD—generalization of Robinsons method, globalized using a filter and trust region;
6) SDPEN—sequential penalty derivative-free method for nonlinear constrained optimization.

A detailed description of each algorithm can be found in [13]. The optimizer comparison strategy consisted of a two-stage optimization strategy as proposed in [11]. A simplified version of the strategy is illustrated in Fig. 7. The strategy consisted of an initial T_A maximization, step O_1, optimizing all the variables

$$X_1 = [X_R \quad X_S]^T \tag{13}$$

as in Table III, with each optimizer starting with identical initial values. In this comparison study, only the four-pole, frame-size 90 dimensions (see Table II) were implemented in the optimization strategy. The rotor topology consisted of four-flux barriers.

The second step, O_2, consisted of a T_R minimization, implementing the best-performing optimized variables of step O_1 as initial variables. Only the barrier tip variable, X_2 in Table III

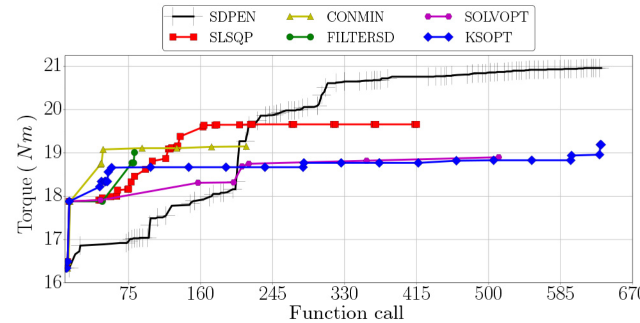

Fig. 8. Optimization study to compare optimization algorithms for step O_1 in Fig. 7 of frame-size 90 machine.

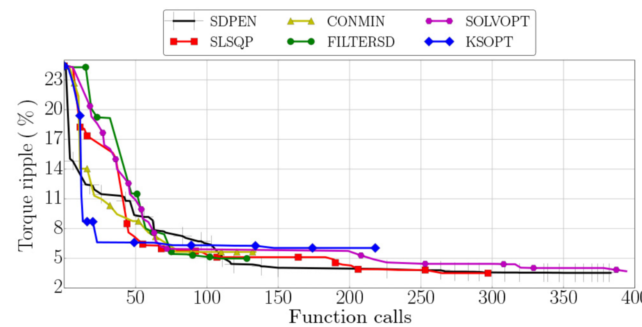

Fig. 9. Optimization study to compare optimization algorithms for step O_2 in Fig. 7 of frame-size 90 machine.

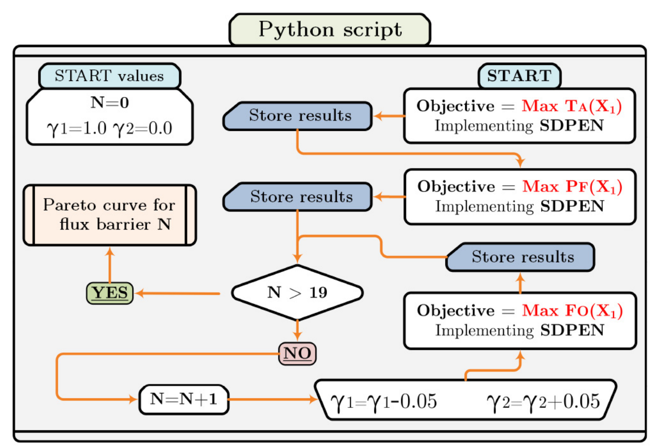

Fig. 10. Weighted-sum model optimization flow diagram.

[see also Fig. 3(a)], was allowed to vary with

$$X_2 = [\alpha_{RL}]. \tag{14}$$

The results of this investigation are shown in Figs. 8 and 9. The gradient step size for each algorithm was determined from iterative identical optimizations implementing the specific optimizer with a variation in step size. The algorithm-selection criteria were based on robustness, optimum solution point repeatability, and a low function-call number for convergence.

Fig. 8 shows that the SDPEN algorithm clearly outperforms the gradient-based algorithms; a much higher optimum objective is reached in roughly 600 function calls. This algorithm was, therefore, selected for step one in the optimization strategy that was implemented in the weighted-factor optimization

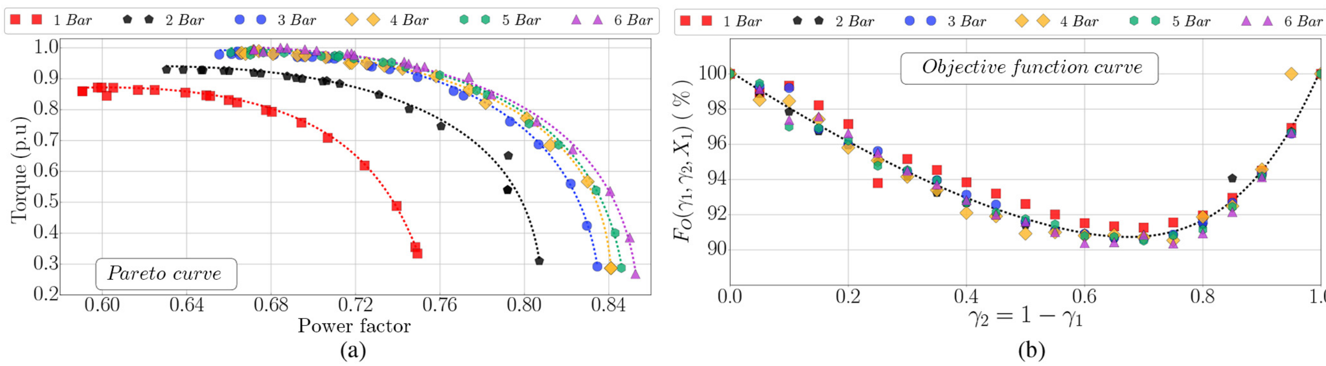

Fig. 11. Multiobjective, weighted-factor optimization results of the 90-frame, four-pole machine. (a) Weighted-factor pareto front. (b) Weighted-factor objective plot versus P_F weight.

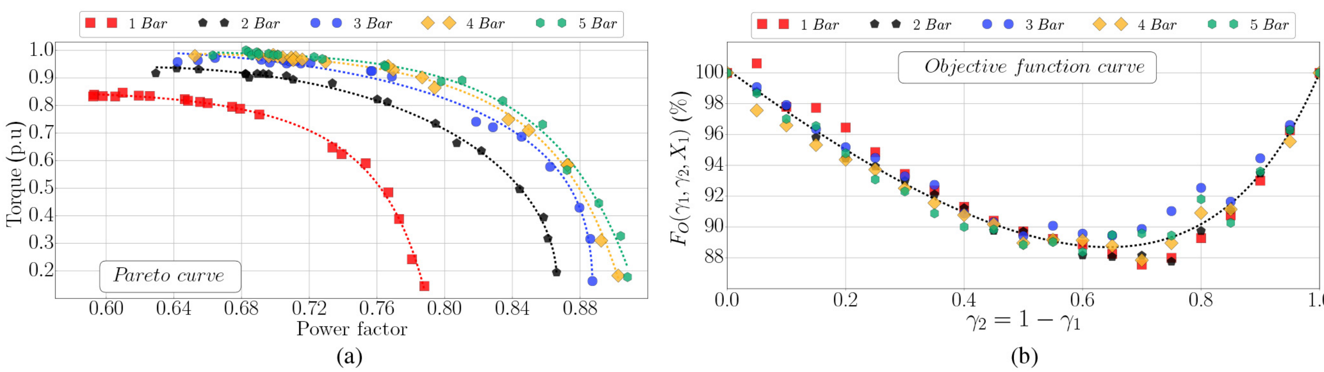

Fig. 12. Multiobjective, weighted-factor optimization results of the 132-frame, four-pole machine. (a) Weighted-factor pareto. front. (b) Weighted-factor objective plot versus P_F weight.

study. The results of the second algorithm study are shown in Fig. 9. This figure shows a more competitive performance of the algorithms, explained by the large reduction in optimization variables compared to the variable count of step O_1. From these results, two algorithms, SLSQP and SDPEN, show clear performance advantages over the others, with a more optimum convergence point achieved in the least amount of function calls. After a comparison of these two algorithms, SLSQP was selected for the second T_R minimization step in the optimization strategy.

For each optimization, in order to avoid objective function contour distortion, each variable was scaled, with the variable inequality constraint consisting of

$$0 \leqslant G(X_m) \leqslant 1 \tag{15}$$

with m, the specific variable set implemented in the optimization.

V. Weighted-Sum Optimization

A. Weighted-Factor Strategy and Results

After the desired optimizer was selected, the multiobjective weighted-sum optimization between T_A and P_F was conducted. The optimization flow diagram is shown in Fig. 10. To accurately scale the weighted-sum objective, each of the respective subobjectives was scaled to its per-unit value with

$$F_O(\gamma_1, \gamma_2, X_1) = \gamma_1 \left(\frac{T_A(X_1)}{T_A(X_1)_{\max}} \right) + \gamma_2 \left(\frac{P_F(X_1)}{P_F(X_1)_{\max}} \right) \tag{16}$$

where $T_A(X_1)_{\max}$ and $P_F(X_1)_{\max}$ are determined, respectively, by maximizing the objective functions

$$F_O(1, 0, X_1) = (1)T_A(X_1) + (0)P_F(X_1) \tag{17}$$

and

$$F_O(0, 1, X_1) = (0)T_A(X_1) + (1)P_F(X_1). \tag{18}$$

These two initial optimization steps are shown in Fig. 10. The weighted pareto-front optimization was then completed by shifting the respective weight from one objective to the other in 19 iteration steps. This strategy, in turn, was repeated for all the machines listed in Table II; hence, the flow diagram shown in Fig. 10 was repeated for each machine pole and flux-barrier number combination.

The optimization results for the four machine configurations, implementing the varying flux-barrier numbers, are shown in Figs. 11–14. The results of each machine consist of the pareto front for each flux-barrier number and the objective function curve for each weighted objective optimization. It is clearly seen, from all the optimized machines, that there is a gradual increase in the pareto ratio between T_A and P_F as the flux-barrier number increases. This increase is initially large from

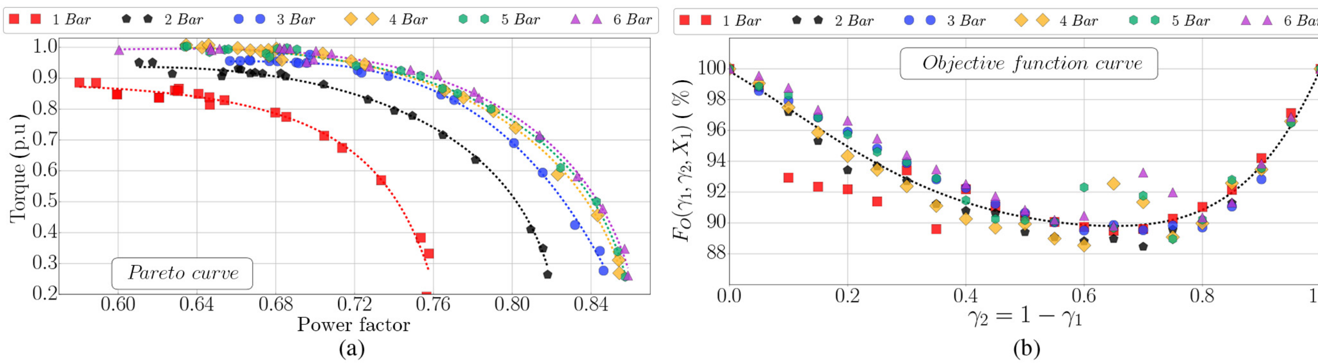

Fig. 13. Multiobjective, weighted-factor optimization results of the 132-frame, six-pole machine. (a) Weighted-factor pareto front. (b) Weighted-factor objective plot versus P_F weight.

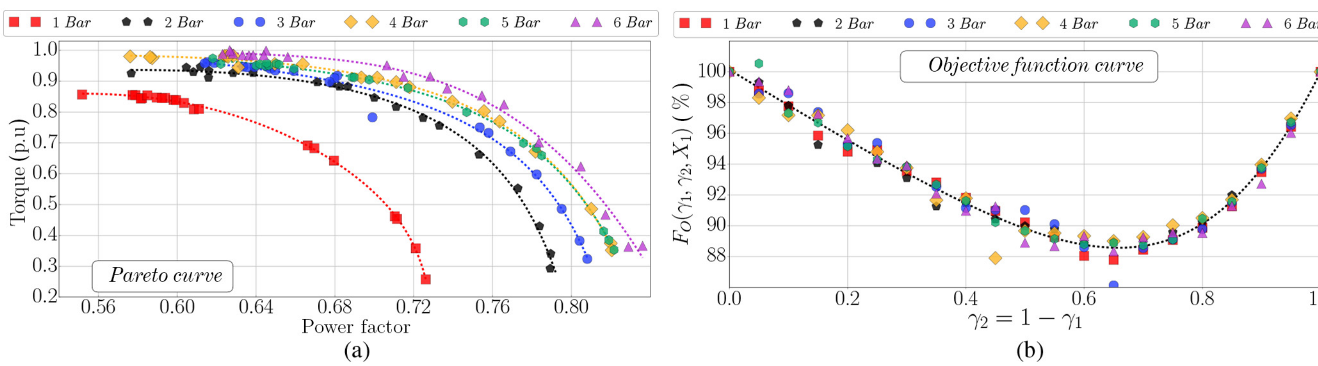

Fig. 14. Multiobjective, weighted-factor optimization results of the 132-frame, eight-pole machine. (a) Weighted-factor pareto front. (b) Weighted-factor objective plot versus P_F weight.

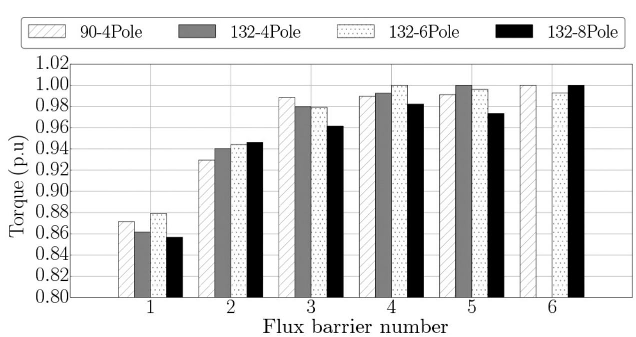

Fig. 15. Maximized objective function $T_A(X_1)_{\max}$ for all machines listed in Table II.

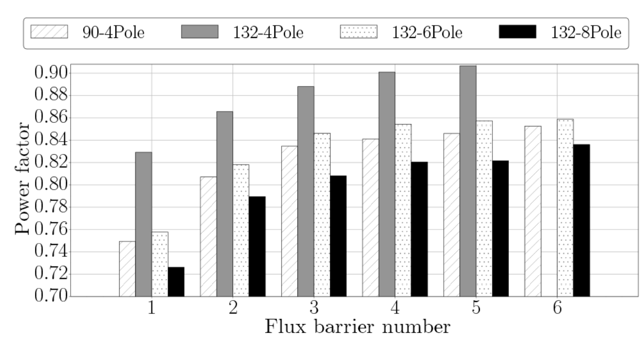

Fig. 16. Maximized objective function $P_F(X_1)_{\max}$ for all machines listed in Table II.

one-flux barrier to two, followed by a steady decrease in pareto ratio as the flux-barrier number increases.

Furthermore, when analyzing the objective curves [see Figs. 11(b)–14(b)], it is evident that the weighted-sum objective results are not flux-barrier-number-dependent, with the objective function results represented by a single curve. Results of the initial two maximized objective functions $T_A(X_1)_{\max}$ and $P_F(X_1)_{\max}$ are presented in the bar charts in Figs. 15 and 16. These figures show the clear increase in T_A and P_F as the flux-barrier number increases, with this increasing trend converging around the four-flux-barrier mark.

To determine a possible global weighted-factor relationship, the results of each machine topology and flux-barrier number combination were normalized by implementing equations

$$T_A(N, X_1)_R = \frac{T_A(X_1)_N - T_A(X_1)_{\min}}{T_A(X_1)_{\max} - T_A(X_1)_{\min}} \tag{19}$$

and

$$P_F(N, X_1)_R = \frac{P_F(X_1)_N - P_F(X_1)_{\min}}{P_F(X_1)_{\max} - P_F(X_1)_{\min}} \tag{20}$$

with N, the step in Fig. 10, and R is the calculated "ratio." $P_F(X_1)_{\min}$ and $T_A(X_1)_{\min}$ in (19) and (20) are the T_A and P_F values, respectively, from the $T_A(X_1)_{\max}$ and $P_F(X_1)_{\max}$ objective designs.

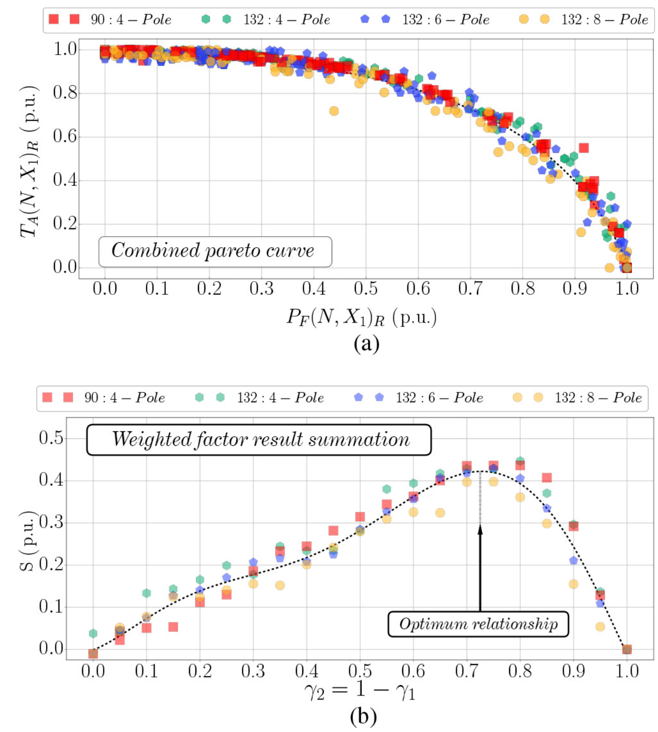

Fig. 17. Scaled weighted-factor optimization results of the designs of the RSMs of Table II. (a) Per-unit pareto front representing the RSMs investigated. (b) Weighted-factor relationship versus P_F weight.

The results of these calculations are shown in Fig. 17(a), i.e., with the normalized pareto front according to (19) and (20) plotted for all the machines and flux-barrier number combinations of Table II. The curve-fit equation for this pareto front consists of

$$y = \frac{a}{\sqrt{b^2 - x^2}} + c \tag{21}$$

with $a = -1.26087$, $b = 1.17596$, $c = 2.06220$ and with the variables x and y representing P_F and T_A, receptively.

This fitted curve illustrates that a power-level, pole, and flux-barrier-number-independent equation exists, which represents the per-unit weighted-factor pareto curve of the objective functions $T_A(X_1)$ and $P_F(X_1)$. This curve equation can consequently be implemented to predict weighted-factor machine optimization performance without having to map the pareto front, with only the maximized $P_F(X_1)_{\text{max}}$ and $T_A(X_1)_{\text{max}}$ to be determined.

In order to increase the accuracy of the prediction, the mean estimated values for each of the respective weights are tabulated in Table IV. The mean estimates x_{mean} and y_{mean} were calculated from the optimized results implementing the optimization weights γ_1 and γ_2 for all the machine combinations given in Table II.

The design estimation process implementing Table IV's results is presented in the flow diagram in Fig 18. The estimation steps consist of:

1) the initial independent maximization to determine $T_A(X_1)_{\text{max}}$ en $P_F(X_1)_{\text{max}}$;

TABLE IV
WEIGHTED-FACTOR MEAN ESTIMATE AND 95% CONFIDENCE INTERVAL FOR OBJECTIVE FUNCTIONS $T_A(X_1)$ AND $P_F(X_1)$

Objective weights		Mean estimate ♠		95% confidence♠	
P_F	T_A	P_F	T_A	P_F	P_F
γ_2	γ_1	x_{Mean}	y_{Mean}	x_{Low}	x_{High}
0.0	1.00	0.00000	1.00000	0.00000	0.00000
0.05	0.95	0.04034	1.00306	0.00000	0.11015
0.10	0.90	0.08796	0.99430	0.00000	0.22598
0.15	0.85	0.11712	0.99202	0.00000	0.32116
0.20	0.80	0.14110	0.99191	0.00000	0.28819
0.25	0.75	0.16569	0.98993	0.00000	0.30960
0.30	0.70	0.18946	0.99193	0.00000	0.28700
0.35	0.65	0.22863	0.98015	0.06402	0.40772
0.40	0.60	0.24385	0.97708	0.05051	0.35162
0.45	0.55	0.28125	0.96744	0.09683	0.38539
0.50	0.50	0.33501	0.95714	0.14551	0.88607
0.55	0.45	0.40894	0.93277	0.26461	0.48832
0.60	0.40	0.44828	0.91253	0.26024	0.58189
0.65	0.35	0.52184	0.86932	0.34583	0.66851
0.70	0.30	0.62934	0.79853	0.51163	0.75531
0.75	0.25	0.69336	0.73750	0.58843	0.80128
0.80	0.20	0.77700	0.64090	0.70459	0.83891
0.85	0.15	0.86359	0.49053	0.79137	0.91992
0.90	0.10	0.93959	0.29720	0.88075	0.98673
0.95	0.05	0.98208	0.12585	0.93615	1.00000
1.00	0.00	1.00000	0.00000	1.00000	1.00000

♠: Equation (21) mean estimate variables and confidence.

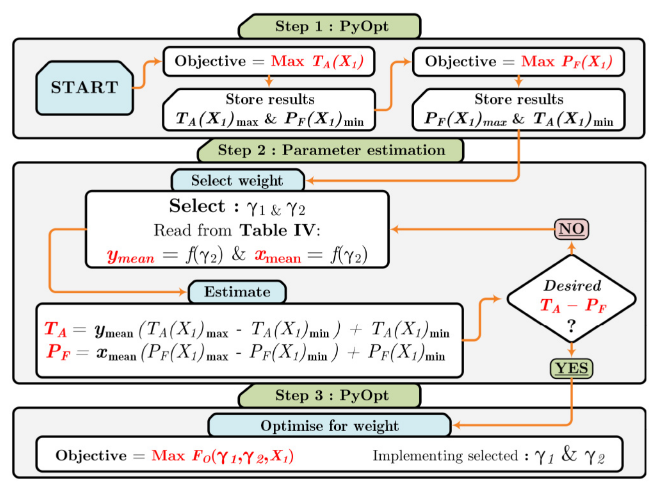

Fig. 18. Weighted factor T_A and P_F estimation step flow diagram.

2) the iterative estimation of T_A and P_F calculated by rewriting (19) and (20) to

$$T_A = y_{\text{mean}}(T_A(X_1)_{\text{max}} - T_A(X_1)_{\text{min}}) + T_A(X_1)_{\text{min}} \tag{22}$$

and

$$P_F = x_{\text{mean}}(P_F(X_1)_{\text{max}} - P_F(X_1)_{\text{min}}) + P_F(X_1)_{\text{min}} \tag{23}$$

with

$$x_{\text{mean}} = f(\gamma_2) \tag{24}$$
$$y_{\text{mean}} = f(\gamma_1) \tag{25}$$

read from Table IV;

TABLE V
ESTIMATED AND OPTIMIZED RESULTS OF 50 Hz RSMs DESIGNED, IMPLEMENTING WEIGHTED FACTOR $\gamma_1 = 0.30$ AND $\gamma_2 = 0.70$

N	P	B	M_W	Estimated T_A (Nm)	Estimated P_F ( )	Optimized T_A (Nm)	Optimized T_A (p.u.)	Optimized P_F ( )	Optimized P_F (p.u.)
[1]♠	Theoretical true estimated $\gamma_1 = 0.30$ and $\gamma_2 = 0.70$								
Asymmetric rotor (h = 2.5 mm ; J = 4.0 A/ mm^2)									
[2]♠	8★	4	9-9	116.1k	0.726	108.7k	0.936	0.743	1.023
[3]♠	8★	4	8-9	117.5k	0.723	110.0k	0.936	0.742	1.026
[4]♠	8★	4	7-9	117.5k	0.723	105.2k	0.895	0.747	1.033
[5]♠	10◇	4	9-9	117.6k	0.726	108.9k	0.926	0.739	1.018
[6]♠	10◇	4	8-9	118.1k	0.729	107.1k	0.907	0.745	1.022
[7]♠	10◇	4	7-9	117.6k	0.729	105.1k	0.894	0.745	1.022
Symmetric rotor (h = 0.3 mm; J = 6.4 A/ mm^2)									
[8]♠	4	6	6-6	17.65	0.781	18.29	1.036	0.776	0.994
[9]♠	6	5	6-6	18.61	0.726	18.31	0.984	0.729	1.004
IM retrofit (h = 0.3 mm ; J = 6.4 A/mm^2)									
[10]♠	4	4	6-6	10.17	0.785	10.23	1.006	0.783	0.998

♠: plotted estimate versus optimized results in Fig. 19; N: machine number in Fig. 19; B: flux barrier number; P: number of poles; h: air-gap height; J: current density; M_W: machine winding; ★: machine volume: (L_S = 2.14 m; ST$_O$ = 0.565 m; $R0_I$ = 0.24 m); ◇: machine volume: (L_S = 1.23 m; ST$_O$ = 0.715 m; $R0_I$ = 0.332 m) .

3) if the desired T_A and/or P_F values are reached, the correlating weighted factors are used in the objective function (16) to optimize the design of the machine.

This optimization prediction is subject to the following optimization machine model constraints:

1) RO$_O \leqslant \frac{3}{4} ST_O$;
2) $\theta_{P_3} \leqslant \theta_{P_1}$;
3) RO$_I$ is fixed;
4) no center flux-barrier web support;

with RO$_O$, ST$_O$, and RO$_I$ shown in Fig. 20, and with θ_{P_1} and θ_{P_3} shown in Fig. 4 and Table I.

B. Define Possible Optimum

To define an "optimum" weighted relationship between the two objectives, the respective *x*- and *y*-axes results of Fig. 17(a) area summarized with

$$S(X_W) = \frac{\sum_1^b T_A(N, X_1)_R}{b} + \frac{\sum_1^b P_F(N, X_1)_R}{b} - 1 \quad (26)$$

with b the number of barrier-number combinations optimized per machine setup and with the "-1.0" value implemented to zero the relationship at the $T_A(X1)_{\text{max}}$ or $P_F(X1)_{\text{max}}$ point. This calculated summation is shown in Fig. 17(b). The optimum relationship between T_A and P_F is also illustrated, with the optimum point between $0.25 \leqslant \gamma_1 \leqslant 0.30$ and $0.70 \leqslant \gamma_2 \leqslant 0.75$.

C. Verification of Weighted-Factor Pareto

To verify the weighted-factor pareto estimation in Fig. 18, nine machines were optimized implementing the weighted factor $\gamma_1 = 0.30$ and $\gamma_2 = 0.70$ ($x_{\text{mean}} = 0.62934$ and $y_{\text{mean}} =$

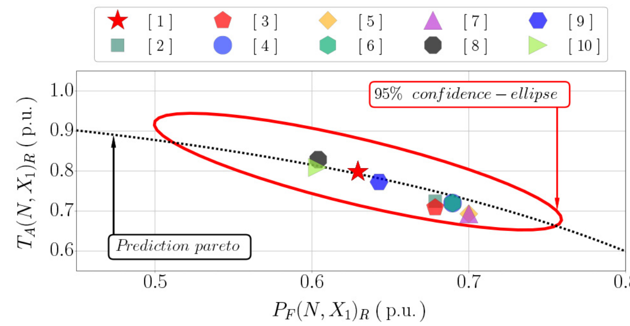

Fig. 19. Pareto plots of optimum designed RSMs 2–10 of Table V compared to the theoretical estimated pareto plot of RSM 1, with 95% confidence ellipse shown.

0.79853 from Table IV). The first six machines optimized included machines in the 100 kNm range, with 8- and 10-pole configurations and having different chorded, overlap winding layouts.

The optimum designed RSMs numbered 8 and 9 in Table V are again small RSMs (90 frame size in Table II), but this time, with symmetric rotor structures. This was done to include also a symmetric rotor structures in the verification study.

The final machine consisted of an induction machine stator retrofit RSM rotor optimization, with a four-flux-barrier rotor optimized. The frame-size dimensions for this machine closely correlate the frame-size 90 dimensions in Table II.

The estimated and actual performances of the design-optimized RSMs are given in Table V, which show, in general, very good comparison for TA and PF. The estimated and actual result points of the RSMs are shown in Fig. 19. This good comparison shows that the theoretical estimated pareto curve not only applies to small RSMs with asymmetric rotors but also to:

1) RSMs with symmetric rotors;
2) RSMs in the very high 100 kNm torque range;
3) RSMs with induction machine stators and retrofit RSM rotors; and
4) RSMs with varying chorded overlap windings.

The deviation from the estimated values obtained for the 100 kNm machines is larger than for the smaller machines. This larger deviation is attributed to the large increase in model size, the increase of air-gap height to a more realistic 2.5 mm, and an increase of the flux-barrier web width to 2.5 mm.

D. Machine Selection and Torque Ripple Reduction

To validate the calculated parameters and investigate the implementation of a high-pole RSM, the eight-pole, four-flux-barrier machine implementing the 132 frame in Table II is selected with weighted factor $\gamma_1 = 0.45$ and $\gamma_2 = 0.55$. This selection was motivated by the desire to investigate RSMs operating in the medium speed range, with the medium speed range falling between 320 and 680 r/min [14]. Furthermore, four-flux barriers were selected after an increase in flux-barrier number to five and six found no significant increase in the T_A–P_F relationships, as seen in Fig. 14(a). The eight-pole, four-flux-barrier RSM selected is shown in Fig. 20.

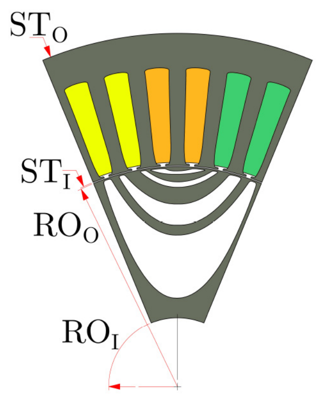

Fig. 20. Pareto curve selected eight-pole, 48-slot RSM with $RO_O = 65.39$ mm, $RO_I = 20.5$ mm, $ST_O = 105$ mm, and stack length 0.12 m, with air-gap length 0.35 mm.

TABLE VI
TORQUE RIPPLE REDUCTION OF THE SELECTED EIGHT-POLE MACHINE

		$\gamma_1 = 0.45 : \gamma_2 = 0.55$ - Optimization results								
Objective function		$F_O(\gamma_1, \gamma_2, X_1)$ $T_A^{\blacktriangle}$	$T_R^{\blacktriangledown}$	$P_F^{\blacktriangle}$	$T_R(X_2)$: 62° $T_A^{\blacktriangle}$	$T_R^{\blacktriangledown}$	$P_F^{\blacktriangle}$	$T_R(X_2)$: 70° $T_A^{\blacktriangle}$	$T_R^{\blacktriangledown}$	$P_F^{\blacktriangle}$
θ		62°	68°	70°	62°	63°	70°	64°	70°	71°
T_A	[Nm]	82.5	80.0	77.4	81.8	81.6	76.0	82.4	79.8	78.5
	[p.u.]	**1.0**	0.97	0.94	0.99	0.99	0.92	1.0	0.97	0.95
T_R	[%]	12.3	10.5	10.6	5.8	5.1	9.2	8.0	5.1	5.2
	[p.u.]	1.17	**1.0**	1.01	0.55	0.49	0.88	0.76	0.49	0.50
P_F	[ ]	0.69	0.72	0.72	0.68	0.69	0.71	0.69	0.72	0.72
	[p.u.]	0.96	1.0	**1.0**	0.94	0.96	0.99	0.96	1.0	1.0

▲: maximum point; ▼: minimum point.

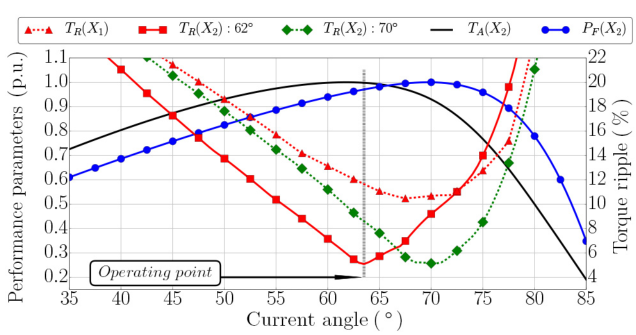

Fig. 21. Average torque, torque ripple, and power factor versus current angle of the selected eight-pole RSM (performance parameters representing T_A and P_F as per unit values).

To reduce the T_R of the selected machine to acceptable levels, the second step of the asymmetric optimization technique in Fig. 6, step O_2, was implemented. This step includes the minimization of the objective function $T_R(X_2)$ by only implementing the asymmetric flux-barrier tip angles. This minimization was done at two fixed current-angle points, 62° and 70°, respectively, with the designer free to select either the peak T_A or P_F operating point for the minimization.

Table VI and Fig. 21 show the minimization results, with the initial results of (16) compared to the two possible current-angle minimization points. For this specific machine, the current angle of 62° was selected for the desired maximum-torque operating point. Table VI clearly shows that there is small, or no, reduction in T_A during the $T_R(X_2)$ minimization, with a $>50\%$ reduction in torque ripple to an acceptable 5.1% at a 63° current angle.

TABLE VII
STRESS AND DEFORMATION ANALYSIS DONE IN JMAG AND ALGOR MULTIPHYSICS ON THE SELECTED EIGHT-POLE RSM

Stress and Deformation analysis						
			JMag		Algor	
Speed★ (p.u)	Temp♣ (°C)	E-M♠	Mises $^{\Re}$ (MPa)	Def * (μm)	Mises $^{\Re}$ (MPa)	Def * (μm)
6	20	NA	93.9	8.56	102.9	8.82
6	20	√	135.0	13.9	NA	NA
6	150	NA	93.9	108.9	102.9	109.2
6	150	√	135.0	114.6	NA	NA

Lamination M470-50A yield strength: 300 MPa; ♣: lamination temperature; ★: speed = 6 × 450 r/min = 2700 r/min; ♠: electromagnetic forces; $\Re$: Von Mises peak stress; *: maximum point deformation.

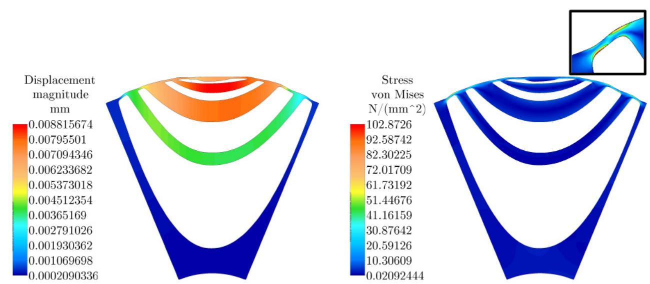

Fig. 22. Stress and deformation analysis, and comparison between structural analysis done in JMag and Algor Multiphysics on the selected eight-pole RSM rotor.

VI. MACHINE MANUFACTURING AND TESTING

Prior to the final machine manufacturing, an extensive structural analysis was conducted on the rotor lamination under rated conditions to determine the structural rigidity. The structural analysis is done using JMAG and Algor simulation packages. Due to the electromechanical simulation limitations of Algor, the initial simulation verification consisted only of a centrifugal force analysis at six times the rated speed (2700 r/min), with the lamination at 20 ° C and 150 ° C temperatures. The structural analysis in JMag was conducted on a 2-D model, whereas a 3-D model was implemented in Algor. This explains the more realistic higher stress and deformations results obtained in Table VII.

After this initial model verification, the simulation was repeated in JMag with inclusion of the electromechanical forces at rated conditions. The structural analysis results are presented in Table VII and Fig. 22. The results in Table VII clearly show that the forces at the extreme conditions are well within the structural limit of the rotor lamination material.

The manufactured rotor and stator are shown in Fig. 23. The machine manufactured RSM had an important difference to the simulated machine, i.e., the stack length of 110 mm was increased to 120 mm. The reason for this increase in stack length was that the machine manufacturer was able to utilize

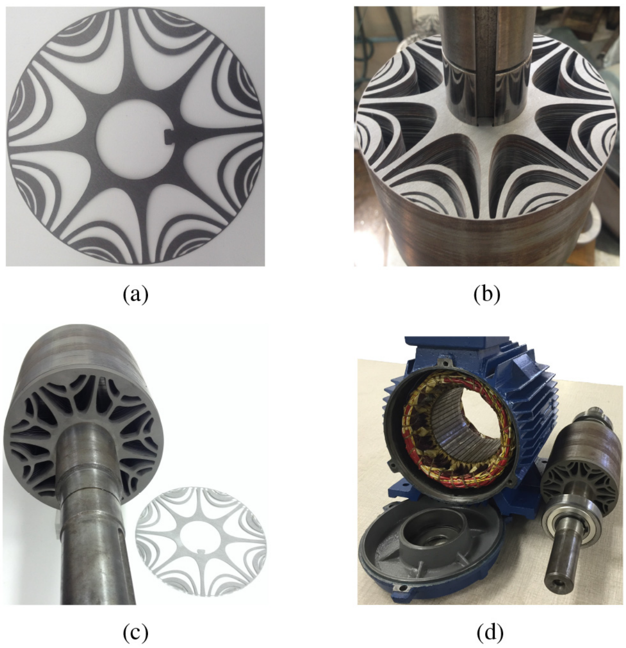

Fig. 23. Rotor and stator manufacturing with the (a) rotor lamination, (b) rotor assembly, (c) completed rotor assembly with end caps, and (d) completed machine assembly.

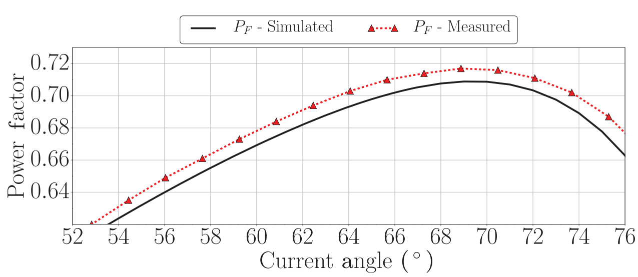

Fig. 24. Measured and simulated power factor versus current angle at 450 r/min at 12.0 A_{rms} with $L_S = 120$ mm.

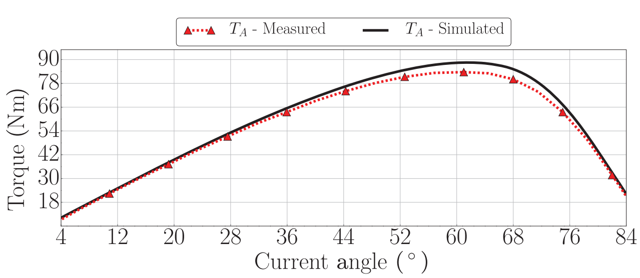

Fig. 25. Measured and simulated average torque versus current angle at 100 r/min at 12.0 A_{rms} with $L_S = 120$ mm.

the machine frame-size volume more effectively. The increase in stack length, however, increased the simulated torque of 81.6 Nm in Table VI to 88.5 Nm at a current angle of 63°.

The simulated and measured power factor of the manufactured machine is shown in Fig 24. At peak power factor, the simulated result of 0.709 closely correlates with the measured power factor of 0.717. In Fig. 25, the measured average torque of the manufactured RSM is compared to the simulated average torque. The measured average torque agrees well with the simulated torque, with the peak simulated average torque of 88.5 Nm compared to the measured average torque of 83.7 Nm.

VII. Conclusion

In this paper, a weighted-factor, multiobjective optimization technique was implemented in the multiobjective optimization of RSMs. This multiobjective optimization was conducted on a large range of machine pole number, flux-barrier number, and power-level combinations.

By implementing the weighted-factor optimization technique, a relationship between power factor and average torque for a RSM was determined. This relationship was proven to be flux-barrier number, pole number, and power-level-independent. Moreover, it was found that this relationship can be used for prediction of optimization results, with the power factor and average torque successfully estimated for a large variation of machine-design configurations within a 95% confidence level. This relationship gives the designer the ability to estimate average torque and power factor at a specific weight point, thus allowing for weighted-factor adjustment to achieve the average torque and power factor relevant to a specific application.

An eight-pole, four-flux-barrier RSM was selected for manufacturing to validate the simulated performance results. The torque ripple of the selected machine was successfully reduced to about 5% by using the technique described in [11].

With the rotor proven to be mechanically sound under rated conditions, the RSM was manufactured and tested. The measured torque and power factor results compared well with the simulated values, with a 1.1% difference in the peak power factor and a 5.4% difference in the peak average torque.

References

[1] M. Gamba, G. Pellegrino, and F. Cupertino, "Optimal number of rotor parameters for the automatic design of synchronous reluctance machines," in *Proc. 21th Int. Conf. Elect. Mach. (ICEM'14)*, Sep. 2014, pp. 1334–1340.

[2] T. Lange, B. Kerdsup, C. Weiss, and R. De Doncker, "Torque ripple reduction in reluctance synchronous machines using an asymmetric rotor structure," in *Proc. 7th IET Int. Conf. Power Electron., Mach. Drives (PEMD'14)*, Apr. 2014, pp. 1–5.

[3] M. Palmieri, M. Perta, F. Cupertino, and G. Pellegrino, "Effect of the numbers of slots and barriers on the optimal design of synchronous reluctance machines," in *Proc. Int. Conf. Optim. Elect. Electron. Equip. (OPTIM)*, May 2014, pp. 260–267.

[4] F. Cupertino, G. Pellegrino, E. Armando, and C. Gerada, "A SYR and IPM machine design methodology assisted by optimization algorithms," in *Proc. IEEE Energy Convers. Congr. Expo. (ECCE)*, Sep. 2012, pp. 3686–3691.

[5] F. Cupertino, G. Pellegrino, and C. Gerada, "Design of synchronous reluctance machines with multi-objective optimization algorithms," in *Proc. IEEE Energy Convers. Congr. Expo. (ECCE)*, Sep. 2013, pp. 1858–1865.

[6] N. Bianchi, M. Degano, and E. Fornasiero, "Sensitivity analysis of torque ripple reduction of synchronous reluctance and interior PM motors," in *Proc. IEEE Energy Convers. Congr. Expo. (ECCE)*, Sep. 2013, pp. 1842–1849.

[7] S. Yammine, H. Carole, M. Fadel, S. Desharnais, and L. Calegari, "Synchronous reluctance machine flux barrier design based on the flux line patterns in a solid rotor," in *Proc. 21th Int. Conf. Elect. Mach. (ICEM'14)*, Sep. 2014, pp. 297–302.

[8] M. Kamper, F. van der Merwe, and S. Williamson, “Direct finite element design optimisation of the cageless reluctance synchronous machine,” *IEEE Trans. Energy Convers.*, vol. 11, no. 3, pp. 547–555, Sep. 1996.
[9] R.-R. Moghaddam and F. Gyllensten, “Novel high-performance SYNRM design method: An easy approach for a complicated rotor topology,” *IEEE Trans. Ind. Electron.*, vol. 61, no. 9, pp. 5058–5065, Sep. 2014.
[10] M. Sanada, K. Hiramoto, S. Morimoto, and Y. Takeda, “Torque ripple improvement for synchronous reluctance motor using asymmetric flux barrier arrangement,” in *Proc. 38th IEEE IAS Annu. Meeting*, Oct 2003, vol. 1, pp. 250–255.
[11] E. Howard, M. Kamper, and S. Gerber, “Asymmetric flux barrier and skew design optimization of reluctance synchronous machines,” *IEEE Trans. Ind. Appl.*, vol. 51, no. 5, pp. 3751–3760, Sep./Oct. 2015.
[12] S. Gerber, “A finite element based optimisation tool for electrical machines,” M.S. thesis, Dept. Elect. Electron. Eng., Univ. Stellenbosch, Stellenbosch, South Africa, 2011 [Online]. Available: http://hdl.handle.net/10019.1/6635
[13] R. E. Perez, P. W. Jansen, and J. R. R. A. Martins, “PYOpt: A Python-based object-oriented framework for nonlinear constrained optimization,” *Struct. Multi. Optim.*, vol. 45, no. 1, pp. 101–118, 2012.
[14] E. Abdi *et al.*, “Performance analysis and testing of a 250 kW medium-speed brushless doubly-fed induction generator,” *IET Renew. Power Gen.*, vol. 7, pp. 631–638, Nov. 2013.

Eduan Howard (S’14) received the B.Eng. degree in mechanical engineering from the University of Stellenbosch, Stellenbosch, South Africa, in 2012, where he is currently working toward the Ph.D. (Eng.) degree in electrical engineering.

His current research focus is on reluctance synchronous machines for wind turbine purposes and includes the optimizing of reluctance synchronous machine technologies, including computer-aided design.

Maarten J. Kamper (M’96–SM’08) received the M.Sc. (Eng.) and Ph.D. (Eng.) degrees from the University of Stellenbosch in South Africa, in 1987 and 1996, respectively, in the field of design of induction and reluctance electrical machines.

Since 1989, he has been with the Department of Electrical and Electronic Engineering, University of Stellenbosch, where he is currently a Professor of electrical machines and drives. His research interests include the design optimization and control of electrical machines, currently with the focus on wind generators and industrial and electric vehicle drives.

Prof. Kamper is Associate Editor of the Electric Machines Committee of the IEEE TRANSACTIONS ON INDUSTRY APPLICATIONS. He also serves on the Steering Committee of the International Conference on Electrical Machines (ICEM).